# Spatial–Temporal Variation Characteristics of Water Bodies and Their Climatic Drivers Over the Qinghai–Tibet Plateau in 2002-2020

Chen Hong, Fuyao Zhu, Mengmeng Wang [ID], and Zhengjia Zhang

*Abstract*—The spatial–temporal characteristics of water bodies and their response to climatic factors are significant for the study of the water budget and the ecological environment. As Asia's water tower, the Qinghai–Tibet Plateau (QTP) has abundant surface water bodies, whose distribution and duration are sensitive to climate change. In this article, the surface water of the QTP in the recent 20 years was extracted from Landsat series TM/ETM+/OLI data combined with the Joint Research Centre of European Commission water body dataset. In addition, the temporal and spatial variation characteristics of the surface water area over the QTP were analyzed, and the climatic factors driving its dynamic change were explored based on 13 climatic variables. Results showed the following: First, from 2002 to 2020, the area of permanent water body in QTP increased from about 46 300 km$^2$ to about 54 700 km$^2$, showing the characteristics of increase in the north and decrease in the south. The area of seasonal water area decreased from about 8900 km$^2$ to about 6600 km$^2$, which were characterized by increase in the west and decrease in the east. Second, with 13 climatic variables reflecting the overall, seasonal, and extreme values of climate changes, the annual total precipitation had the strongest effect on the permanent water area over the total QTP, and the autumn mean air temperature was most relevant with the seasonal water area. Third, the predicted permanent water area of the QTP showed a trend of first slow and then fast increasing during 2021–2025, and expanded by 294 km$^2$ in 2025 compared with 2021, whereas the seasonal water area first increased by 131 km$^2$ and then decreased by 203 km$^2$. These results will help provide important references for water resource management and ecological environment protection in QTP.

*Index Terms*—Climate change, landsat series data, Qinghai–Tibet Plateau (QTP), spatiotemporal variation analysis, surface water body extraction.

## I. INTRODUCTION

THE Qinghai–Tibet Plateau (QTP) is located in the middle and low latitudes of the Northern Hemisphere and in Western and Southwestern China. As a main accumulation region of lakes, glaciers, perennial snow, and permafrost, the QTP is a strategic place for the generation, occurrence, and migration of water resources in Asia and even the world [1]. The QTP plays a pivotal role in the formation of the climate characteristics of China and Asia [2]. Research data showed that global climate change is profoundly changing the status, pattern, and service functions of the water system in rivers and lakes (river source areas) in high, cold regions [3], [4]. The distribution and duration of surface water, which is affected by climate and human activities, have an influence on climate, biodiversity, and human well-being [5]. Many researchers have shown that the QTP is experiencing a process of climate warming and humidifying in recent years, resulting in multiyear glacier and snow retreat, and water resource reduction [6], [7], [8]. Therefore, studying the temporal and spatial changes of water bodies in the QTP, and analyzing their climate drivers are significant, which can provide a scientific basis for regional ecological environmental security, social and economic development, management, and planning [9]. Studying the driving mechanism of climatic factors on the water bodies in the QTP is meaningful for the security of regional ecological resources, the protection and exploitation of the ecological environment, the assessment of human existence environment, and the sustainable development of the QTP.

Over the past decades, many studies have been conducted for surface water mapping using remote sensing (RS) data [10], [11], [12], and these methods can be divided into three groups. The first is based on supervised and unsupervised classification. Supervised classification is to select training samples and compare each pixel with them to complete the classification. Unsupervised classification uses different image features in the feature space without a prior classification criterion to complete image classification. This kind of method is inefficient and not suitable for large-scale extraction [13]. The second is to use the single-band threshold method to extract the water body from RS images [14], [15], [16]. The single-band threshold method mainly uses the difference in spectral characteristics between water and other land cover types to distinguish water bodies by setting appropriate thresholds. The method is simple but has a low accuracy [17]. The third is to calculate the water index to

Chen Hong is with the S.K.Lee Honors College, China University of Geosciences, Wuhan 430074, China (e-mail: 20191003449@cug.edu.cn).

Fuyao Zhu is with the School of Geophysics and Geomatics, China University of Geosciences, Wuhan 430074, China (e-mail: 20191001889@cug.edu.cn).

Mengmeng Wang and Zhengjia Zhang are with the School of Geography and Information Engineering, China University of Geosciences, Wuhan 430074, China (e-mail: wangmm@cug.edu.cn; zhangzj@cug.edu.cn).

extract water bodies. Related scholars have constructed many efficient, high-precision water indices through the spectrum response of water bodies. The normalized differential water index (NDWI) can extract water quickly and conveniently with a high accuracy [9], [18], [19]. Compared with NDWI, the modified normalized difference water index (MNDWI) proposed by Xu has a higher accuracy in extracting the water boundary of eutrophic lakes and can easily distinguish shadows from water bodies [20]. Landsat series satellites have provided long-term observations of the Earth since 1972, which present a unique opportunity to provide long-term surface water monitoring at a fine spatial resolution (30–78 m) [21], [22], [23].

Many studies on the spatial-temporal variation of water body and its driving mechanism have been conducted through multiple statistical methods, including correlation analysis, linear trend analysis, Mann–Kendall trend test, and autoregressive integrated moving average (ARIMA) model, in different regions [24], [25], [26], [27], [28]. Liu and Wu [29] and Lid et al. [30] used the above methods to analyze the change of water body by taking the whole study region as the analysis unit. However, these methods are less applicable if the study area is large and highly spatial heterogeneous. Therefore, Geets et al. [31] and Zhu et al. [32] used clustering analysis and rotation empirical orthogonal function to divide the study region into multiple analysis units, and then analyzed each unit using the above methods. Dividing the research region by the watershed unit of the water cycle is also a method to solve the spatial heterogeneity problem. Mason et al. [24], Assel [33], and O'Reilly et al. [34] divided the study area by watershed boundary, and conducted coupling simulation analysis of climatic factors and water resources in each unit.

At present, much effort has been devoted to the analysis of the temporal and spatial distribution of water bodies, and their driving factors in the QTP [35], [36]. Some progresses have been made, but some deficiencies remain. Most of the existing studies use single-phase RS data to extract the water body, which has less representation of the annual water body because the distribution of the water body in the QTP is more sensitive to seasons. Moreover, the analysis of climatic factors in existing studies is often limited to the annual total, annual mean, and annual maximum value of temperature, precipitation, and evapotranspiration, ignoring seasonal variation in the correlation between climatic factors and water bodies. In addition, existing studies rarely investigate the relationship between water body change and climatic factors over the whole of the QTP considering spatial heterogeneity [37], [38]. Different from the existing studies, this article focuses on the large-scale, multi-temporal, and comprehensive study on the water bodies and climatic factors of the QTP, and analyzes the spatial–temporal variation of the water bodies and the coupling response relationship between the water bodies and the climatic factors considering spatial and seasonal variation.

In this article, Landsat 5 (TM), Landsat 7 (ETM+), and Landsat 8 (OLI) satellite images and related climate factor data in the QTP from 2002 to 2020 were used as data sources, and the QTP was divided into 12 analysis units based on the watershed boundary. The MNDWI was used to extract the initial water body

information from the Landsat series data, and water occurrence frequency (WOF) representing how often the water body exists in a year was calculated based on multiphase water body data. On this basis, the characteristics of water body change in time and space over the QTP were analyzed, and the inner driving laws of climatic factors were investigated by 13 climatic variables considering seasonal differences, such as summer mean air temperature and autumn mean air temperature. Finally, the ARIMA model was used to predict the monthly climatic factors over five years, and the change in the area of each water body in the QTP for the next five years was predicted by the linear relationship between the climate factor with the highest correlation and the type of water body.

## II. STUDY AREA AND DATA SOURCES

### A. Study Area

The QTP, known as the "roof of the world" and the "third pole," is the largest plateau in China and the highest plateau in the world. It starts from the southern margin of the Himalayas in the south, extends to the northern margin of the Kunlun Mountains, the Altun Mountains, and the Qilian Mountains in the north, the Pamir Plateau and the Karakoram Mountains in the west, and connects with the western section of the Qinling Mountains and the Loess Plateau in the east and northeast, between $26°00'$ – $39°47'$ N and $73°19'$ – $104°47'$ E, see Fig. 1. The QTP is about 2800 km long from east to west and 300–1500 km wide from north to south, with a total area of $2.5 \times 10^6$ km$^2$. It is the largest river source area in the world and known as the "Asian Water Tower" [39]. The QTP is the highest giant tectonic landform unit in the world with a unique natural environment and spatial differentiation laws. Restricted by atmospheric circulation and plateau topography, the annual average temperature in the interior region of the QTP is below 0 °C, and the warmest monthly average temperature in most areas is less than 10 °C [40]. The average temperature decreases from southeast to northwest, and the annual precipitation correspondingly decreases from 2000 mm to below 50 mm, showing a change from warm and humid in the southeast to cold and arid in the northwest. To highlight the spatial heterogeneity of the QTP, which is divided into 12 subregions based on the watershed boundary, including AmuDayra, Brahmaputra, Ganges, Hexi, Indus, Inner, Mekong, Qaidam, Salween, Tarim, Yangtze and Yellow.

### B. Data Sources

*1) Landsat Data:* Based on the Google Earth Engine platform, Landsat 5 (TM), Landsat 7 (ETM+), and Landsat 8 (OLI) satellite RS data were used to extract surface water information in the QTP [41], [42]. Since July 23, 1972, NASA's Landsat program (known as EARTH Resource Technology Satellite before 1975) has launched eight satellites and continuously acquired the satellite data of land surface for 50 years. Landsat images have a spatial resolution of 30 m and a scan width of about 185 km, with wavelength covering from visible to infrared spectral. A total of 90 126 Landsat images from 2002 to 2020 were used in the article, as shown in Fig. 2. The Landsat satellites consisted of
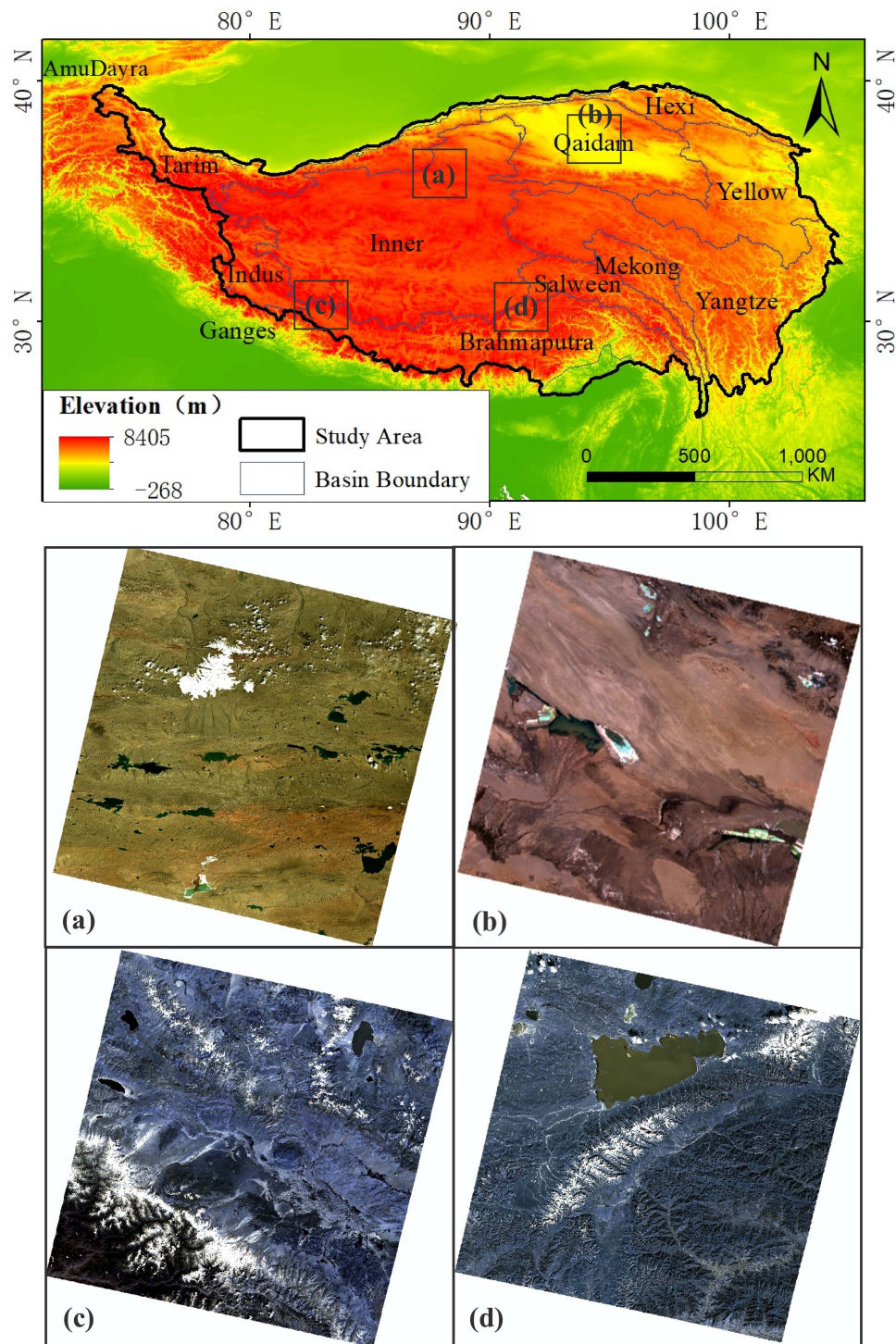
Fig. 1. Topographic conditions and subbasin distribution in the Qinghai–Tibet Plateau, and maps of four Landsat 8 images (Red: band 4, Green: band 3, Blue: band 2) for the accuracy assessment of water body extraction (a–d).

Landsat 5 and Landsat 7 during 2002 to 2011, and the number of Landsat images was between 3000 and 4800. Only one Landsat satellite (i.e., Landsat 7) was available, and the Landsat image number was about 2500 in 2012. After the launch of the Landsat 8 satellite in 2013, the amount of data has been greatly improved. The Landsat image data of the QTP stabilized at more than 6000 scenes for each year after 2014.

*2) Climate Data:* Three climatic factors were employed to investigate the climatic drivers of water body change over the QTP in 2002–2020, including air temperature, precipitation, and evapotranspiration. Monthly air temperature and evapotranspiration data were provided by the meteorological reanalysis data of the European Centre for Medium-Range Weather Forecast (ECMWF) with a temporal resolution of 12 h and a spatial
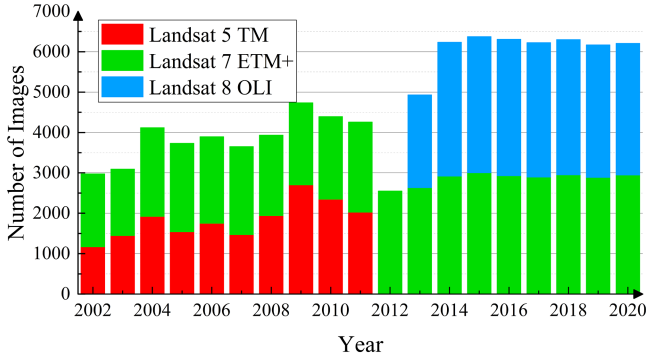
Fig. 2.    Number of Landsat series satellite images used in this article.

resolution of $0.5° \times 0.5°$ [43], [44]. ECMWF meteorological data enable the regular "reanalysis" of archived observations to create a global dataset describing the recent history of weather, land, and ocean, which is available for free on its website.[1] Monthly precipitation data was extracted from the integrated multisatellite retrievals for GPM (GPM IMERG) dataset. GPM is a new generation of global satellite precipitation program jointly developed by the United States, Japan, and other countries. It consists of a core observation platform equipped with a dual-frequency precipitation radar, a microwave imager, and eight partner satellites [45]. It can realize global precipitation observation every three hours with a spatial resolution of $0.1° \times 0.1°$ [46]. GPM IMERG data can be downloaded from the official website of NASA[2] [47]. A total of 13 climatic variables were counted from monthly air temperature, precipitation, and evapotranspiration, namely, annual mean temperature, spring mean temperature (March–May), summer mean temperature (June–August), autumn mean temperature (September–November), winter average temperature (December–next February), mean temperature of the hottest month, mean temperature of the coldest month, annual total precipitation, spring total precipitation, summer total precipitation, autumn total precipitation, winter total precipitation, and annual total evapotranspiration.

## III. METHODS

Landsat 5, 7, and 8 images, ECMWF data, and GPM IMERG data were used as data sources to analyze the spatiotemporal changes of the water body area in the QTP and predict the future changes of the water body area under the influence of climatic factors. The MNDWI was used to extract the initial water body information from the Landsat series data of the QTP in the past 20 years, and the Joint Research Centre of European Commission (JRC) global surface water product was used to filter hill shadow and other misclassifications to improve the accuracy of water body extraction. The change characteristics of the water bodies in time and space were analyzed, and the climatic factors driving their dynamic change were explored using the methods of linear trend analysis, correlation analysis, and time-series analysis. Finally, the ARIMA model was employed to forecast the monthly climatic factors from 2021 to 2025, combining the

correlation analysis, and with further predict the changes in the area of water bodies of the QTP in the next five years. The flowchart of the article is shown in Fig. 3.

### A. Water Classification Based on Long-Term Time-Series Landsat Data

*1) Modified Normalized Difference Water Index:* The MNDWI developed by Xu et al. [20] was used to extract surface water for all Landsat images. Binary conversion was performed based on the MNDWI at the threshold of 0 [48]. The pixel with MNDWI greater than 0 was considered as water, and the pixel with MNDWI less than 0 was considered as nonwater. MNDWI was calculated as follows:

$$\text{MNDWI} = \frac{\rho_{\text{green}} - \rho_{\text{swir}}}{\rho_{\text{green}} + \rho_{\text{swir}}} \quad (1)$$

where $\rho_{\text{green}}$ is the green band surface reflectance of the TM/ETM data, and $\rho_{\text{swir}}$ is the surface reflectance for mid infrared band.

*2) Evaluation of Surface Water Extraction Accuracy:* The visual interpretation method was used to assess the accuracy of surface water extraction using MNDWI. A total of 250 random points were generated for each validating Landsat image to judge whether the classification of random points was correct. For the sample points that were difficult to identify in the Landsat image, high-resolution images with a relatively close time were used to assist the interpretation. Finally, the correct and incorrect classifications were counted, and the overall accuracy was calculated using the following formula:

$$\text{Overall Accuracy} = \frac{A + B}{N} \times 100\% \quad (2)$$

where $A$ is the number of random points identified as water by MNDWI and visual interpretation simultaneously, $B$ is the number of random points identified as nonwater by MNDWI and visual interpretation simultaneously, and $N$ is the total number of random points. The Kappa coefficient was calculated as follows [49]:

$$\text{Kappa} = \frac{p_0 - p_e}{1 - p_e} \quad (3)$$

with

$$p_e = \frac{a_1 \times b_1 + a_2 \times b_2}{N \times N} \quad (4)$$

where $a_1$ and $a_2$ are the number of random points calculated as water and nonwater by MNDWI, respectively; $b_1$ and $b_2$ are the number of random points identified as water and nonwater bodies by visual interpretation, respectively; and $p_0$ is the overall accuracy.

*3) Water Occurrence Frequency Calculation:* Considering that the water distribution data of a single phase representing the water distribution in whole year has certain limitations, the yearly time-series water distribution data were synthesized to obtain the annual WOF data using the following formula:

$$F = \frac{W}{W + \text{NW}} \quad (5)$$

where $W$ is the number of times a pixel is classified as water based on all good observations in a year, NW is the number of

Fig. 3. Flowchart of the analysis of spatial–temporal variation characteristics of the water bodies and their climatic drivers over the Qinghai–Tibet Plateau in 2002–2020.

times a pixel is classified as nonwater, and $F$ is the WOF and is between 0 and 1. Based on the WOF, the pixel was divided into three categories: nonwater body (WOF $< 25\%$), seasonal water body ($25\% <$ WOF $< 75\%$), and permanent water body (WOF $> 75\%$) [50], [51].

### B. Spatial–Temporal Analysis of Water Body

*1) Correlation Analysis:* Pearson correlation coefficient is a statistic that describes the degree of linear correlation between two data [52]. The Pearson correlation coefficients between the area of water bodies (i.e., seasonal water body and permanent water body) and the 13 climate variables were calculated to judge the strength of the correlation between them. The Pearson correlation coefficient can be calculated as follows:

$$ r_{X,Y} = \frac{\text{cov}(X,Y)}{\sigma_X \sigma_Y} = \frac{E[(X - \mu_X)(Y - \mu_Y)]}{\sigma_X \sigma_Y} \quad (6) $$

where $r_{X,Y}$ is the Pearson correlation coefficient between the two data, $X$ and $Y$; $\text{cov}(X,Y)$ is the covariance of the two data; $\sigma_X$ and $\sigma_Y$ are the standard deviations of the two data, $X$ and $Y$,

respectively; $E$ is the variance of the data; $\mu_X$ and $\mu_Y$ represent the average values of the two data, respectively.

The constant $r_p$ can be obtained by consulting the correlation coefficient table. If $|r_{X,Y}| > r_p$, then under the significance level $p$, the water body area or the climate factor variable $x_i$ changes significantly with the time series $t_i$, which can pass the significance test of $p$; otherwise, the change trend is not significant. Generally, $p$ often takes 0.01, 0.05, or 0.001 as the significance level. The smaller the value of $p$ is, the larger the $r_p$, indicating that the change trend is more significant.

*2) Linear Regression Analysis:* Linear regression analysis was employed under three situations in this article.

a) When reflecting the area changes of seasonal water and permanent water bodies with time, $y_i$ represents the water body area, and $x_i$ represents the time.

b) When reflecting the change of climate factor variables with time, $y_i$ represents the climatic variable, and $x_i$ corresponds to the time.

c) When studying the relationship between the water body area and the climate factor variable, $y_i$ represents the water body area, and $x_i$ corresponds to the climate factor variable. The unitary linear relationship between

dependent variables $y_i$ and independent variables $x_i$ was established as follows [53]:

$$y_i = \text{intercept} + \text{slope} \cdot x_i \tag{7}$$

where $i$ represents the sample $i$, $i = 1, 2, \ldots, n$, intercept is a linear regression constant, and slop is a linear tendency coefficient. The values of intercept and slope were determined using the least square method.

*3) Time-Series Forecast of Climatic Factors:* The ARIMA($p$, $d$, $q$) model is the ARIMA model, which treats the data series formed by the predicted objects over time as a random series. The part AR is an autoregressive process, and the part MA is a moving average process [54]. $p$ represents the order of the autoregressive expression, $d$ is the order of differences to make the sequence stationary, $q$ is the order of moving average term [55]. ARIMA($p, d, q$) is typically expressed as shown in the following equation [56], [57]:

$$y_t = \alpha + \varphi_1 y_{t-1} + \varphi_2 y_{t-2} + \cdots \varphi_p y_{t-p}$$
$$+ \varepsilon_t - \theta_1 \varepsilon_{t-1} - \cdots - \theta_q \varepsilon_{t-q} \tag{8}$$

where $y_t$ is current time-series value, accordingly $y_{t-1}, y_{t-2}, \ldots, y_{t-p}$ is the past value. $\varphi_i(i = 1, 2, \ldots, p)$ and $\theta_i(i = 1, 2, \ldots, q)$ are the AR and MA model parameters, $\alpha$ is intercept and also the constant term in the model. $\varepsilon_t$ is the current residual, accordingly $\varepsilon_{t-1}, \varepsilon_{t-2}, \ldots, \varepsilon_{t-p}$ is the past residuals. $\varepsilon_t$ denotes the difference of $y_i$ in two time phases. Three metrics, namely, $R^2$, root-mean-square error (RMSE), and relative root mean square error (r_RMSE) were employed to evaluate the results of ARIMA.

*4) Cumulative Distance Leveling Curve:* To further analyze the cumulative effect of the multiyear changes of climatic factors and the relationship between the water body area and the various climatic factors, the standardized cumulative anomaly curve was extracted over the QTP from 2002 to 2020 for annual mean air temperature, annual total precipitation, and annual total evapotranspiration [58]. The cumulative distance level reflects the phase characteristics of climatic factors by calculating the cumulative distance from the annual value to the multiyear average value. Taking the standardized cumulative anomaly curve of annual mean air temperature as an example, the rising and falling sections of the standardized cumulative anomaly curve represent the relatively warm and relatively cold periods of the QTP temperature, respectively.

## IV. RESULTS

### A. Accuracy Evaluation of Water Extraction

To evaluate the accuracy of the surface water extraction method based on MNDWI, four Landsat images evenly distributed in the QTP were employed (see Fig. 1). These four Landsat images, with different elevations, had large lakes and permanent and seasonal water bodies at the same time, which were representative in the image selection. The overall accuracy and Kappa coefficient calculation results for the four Landsat images are shown in Fig. 4, and the commission error and omission error are given in Table I.
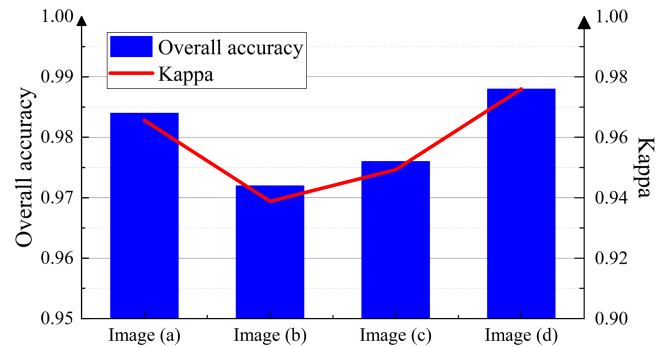


Fig. 4. Overall accuracy and Kappa coefficient of four Landsat images based on the validation with visual interpretation.

TABLE I
COMMISSION ERROR AND OMISSION ERROR OF FOUR LANDSAT IMAGES

| Image | commission error | | omission error | |
|---|---|---|---|---|
| | water | nonwater | water | nonwater |
| 1 | 3.23% | 0.64% | 1.10% | 1.89% |
| 2 | 4.49% | 1.86% | 3.41% | 2.47% |
| 3 | 4.12% | 1.31% | 2.11% | 2.58% |
| 4 | 1.66% | 0.77% | 0.84% | 1.53% |

The accuracy evaluation of the surface water extraction showed that the overall classification accuracies for the four Landsat images were 98.40%, 97.20%, 97.60%, and 98.80%, respectively. The accuracies of images (b) and (c) were slightly lower than images (a) and (d). This is because the water bodies in images (b) and (c) were smaller than that of images (a) and (d) and had more mixed pixels, hence arousing more uncertainty in surface water extraction. In addition, the water bodies in images (b) and (c) were less than those in images (a) and (d). The number of random points falling on the water samples in images (b) and (c) was less, which also affected their accuracy. In general, the method combing the MNDWI with the JRC water body dataset has a high accuracy for surface water extraction over QTP, with overall accuracies of higher than 97%.

For JRC global surface water data, commission errors were less than 1% and omission errors were less than 5% [22]. By comparison, the accuracy of the proposed method in this study is close to the accuracy of JRC global surface water data.

### B. Analysis of Spatial–Temporal Changes in Water Bodies

*1) Spatial Distribution of Water Bodies:* Taking 2020 as an example, the classification map of water bodies in the QTP area is shown in Fig. 5. The water bodies were widespread throughout the QTP and had significant regional differences due to the influence of climate and other factors. The water bodies of the QTP showed the overall characteristics of more in the northern and western parts and less in the southern and eastern parts. Fig. 5(a) shows seasonal water body in the shape of a river inflow in the western part of Achickule lake. As shown in Fig. 5(b) and (c), Qinghai lake and Seling Co lake, as the first and second largest saltwater lakes in the Chinese mainland, have large area of permanent water bodies. In addition, Fig. 5(d) and (e) show
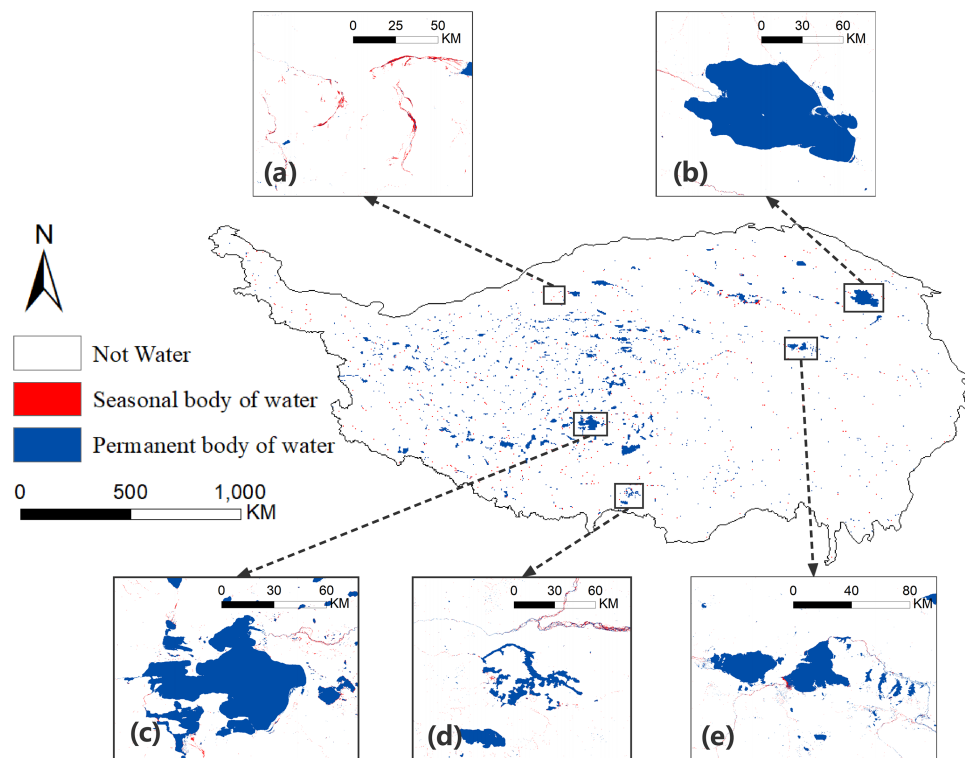
Fig. 5. Classification map of water bodies in the QTP region in 2020. (a) West of Achickule lake. (b) Qinghai lake. (c) Seling Co lake. (d) Pumoyum Co lake and Yamdrok lake. (e) Zhaling lake and Eling lake.

the distribution of water bodies for four lakes in the QTP, i.e., Pumoyum Co lake, Yamdrok lake, Zhaling lake, and Eling lake. They have large scale permanent water bodies, and have small scale seasonal water bodies distributed around the lake.

*2) Water Body-Type Transformation:* Fig. 6 shows the transformation of water body-type over QTP from 2002 to 2020. As shown in Fig. 6(a), the surface water area of Baisha lake in the northwest of the QTP increased rapidly in the past 20 years, mainly as the transformation of some nonwater bodies and seasonal water bodies into permanent water bodies. Zhuonai lake in the middle of the QTP showed a decreasing trend in the water body area, and some permanent water bodies were converted into seasonal water bodies, as shown in Fig. 6(b). In Fig. 6(c), East Dabson Lake had both new water body and disappeared water body. Part of the permanent water bodies in the eastern and western parts of the East Dabson lake disappeared while some new permanent water bodies appeared in the middle. Fig. 6(d) shows an expanding trend of Seling Co lake. The nonwater bodies were transformed into permanent water bodies and seasonal water bodies, which led to the increase of the area of Seling Co lake in recent years. In Fig. 6(e), some nonwater bodies on both sides of the channel of the Yalong river region were converted into permanent water bodies, and the increase in its water volume was reflected in the widening of the river channel. In addition, a small amount of seasonal water bodies was distributed outside the permanent water bodies, reflecting the water body change in the Yalong River with the dry and rainy seasons.

*3) Analysis of Water Body Change Trend:* The area change of seasonal and permanent water bodies with time in the whole

of the QTP was analyzed, as shown in Fig. 7. The permanent water area changed from about 46 300 km$^2$ to about 54 700 km$^2$ from 2002 to 2020, showing a fluctuating upward trend. The permanent water in the QTP had a minimum area in 2002, about 46 300 km$^2$, and reached the maximum in 2019, about 55 600 km$^2$. The permanent water area increased by an average of 432 km$^2$ per year. Seasonal water area changed from about 8900 km$^2$ to about 6600 km$^2$, showing a fluctuating downward trend. Seasonal water area was the largest in 2002, about 8900 km$^2$, and reached the minimum in 2019, about 6400 km$^2$. The average annual reduction of the seasonal water area was 57 km$^2$. Overall, the water body area of the QTP (including seasonal and permanent water bodies) in 2002 was about 55 200 km$^2$, accounting for 2.19% of the total area of the QTP. In 2020, the water body area (including seasonal water and permanent water) was about 61 300 km$^2$, accounting for 2.43% of the total area of the QTP, and the overall water area had a fluctuating upward trend.

The temporal and spatial variation of water bodies for 12 subbasins in QTP was further analyzed, as shown in Figs. 8 to 10. Fig. 8 shows that the permanent water body area of most basins was increasing. Fig. 10 shows that the permanent water area of Inner basin increased significantly at a rate of 297 km$^2$/a, and the permanent water area of Salween basin decreased significantly at a rate of 2.40 km$^2$/a. From the perspective of spatial location, the regions increased with high significance in permanent water body area were mostly located in the northern, western and eastern parts of the QTP, whereas the four basins with decreasing trend of permanent water body area were located in the southwestern part of the QTP. Fig. 9 shows that the seasonal water area
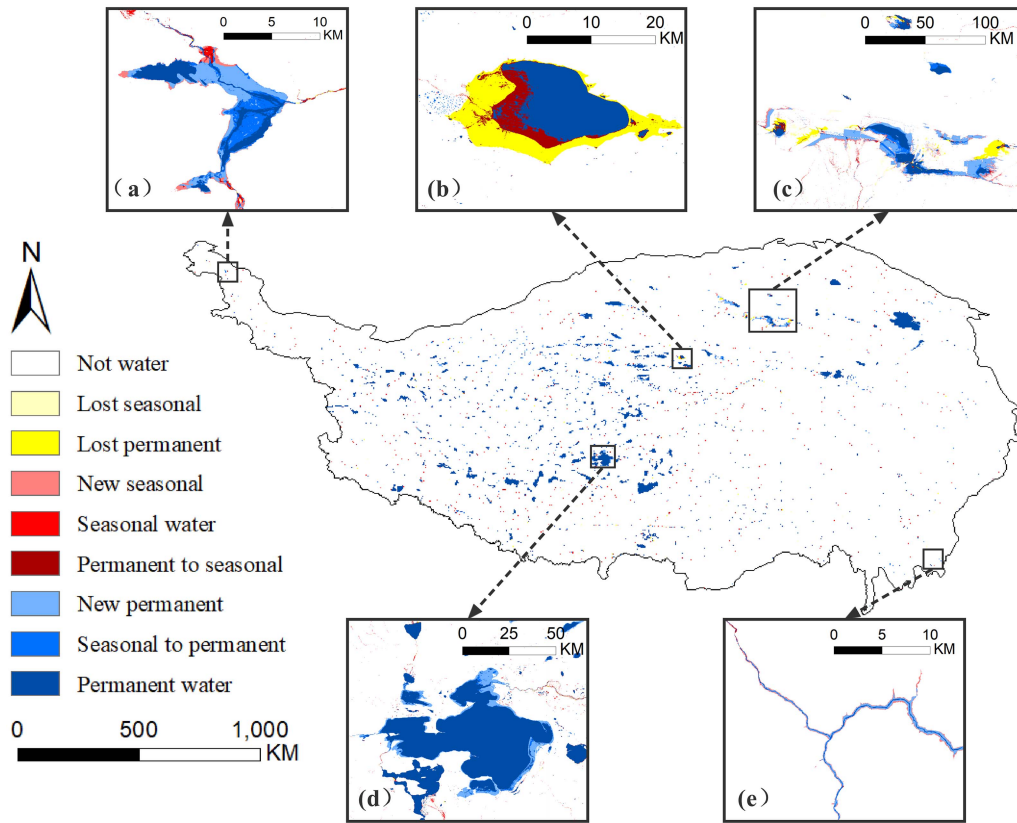
Fig. 6.    Map of water body-type conversion in the QTP from 2002 to 2020. (a) Baisha lake. (b) Zhuonai lake. (c) East Dabson lake. (d) Seling Co lake. (e) Yalong river.
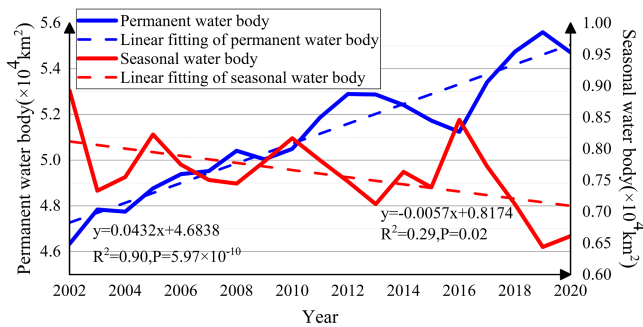


Fig. 7.    Interannual changes of permanent and seasonal water bodies area in QTP from 2002 to 2020.

of Indus basin increased significantly at a rate of 1.60 km$^2$/a, and the seasonal water area of Inner basin decreased significantly at a rate of 52 km$^2$/a. From the perspective of spatial location, the regions increased with high significance in seasonal water body area were mostly located in the central part of QTP, whereas the regions with a decreasing trend of the seasonal water body area were located in the Eastern QTP.

### C. Statistical Analysis and Time-Series Analysis of Climatic Factors

*1) Statistical Analysis of Climatic Factors:* The average temperature, annual precipitation, and annual evapotranspiration of the QTP from 2002 to 2020 are shown in Fig. 11. On the time

scale, the average temperature, annual precipitation, and annual evapotranspiration of the QTP in the past 20 years showed a fluctuating upward trend. The average temperature of the QTP had the most obvious increasing trend with the interannual variation based on the relative rate of factor change (the ratio of the absolute rate of change to the mean value of the factor for many years), increasing at the rate of 0.0232 °C/a. The changes of annual precipitation and annual evapotranspiration were relatively slow, increasing slowly at the rates of 2.0837 mm/a and 0.1458 mm/a, respectively. The three climatic factors in the QTP had 4–5 fluctuations in the time-frequency domain in the past 20 years. The average temperature and annual evapotranspiration showed the same trend, which was consistent with the physical law of higher temperature and faster evaporation. In 2016, the sum of annual average temperature and annual evapotranspiration reached the maximum in nearly 20 years, namely, −2.232 °C and 412.577 mm, respectively.

Fig. 12 shows that in 2005–2007 and 2014–2015, temperature and evapotranspiration increased, whereas precipitation decreased, corresponding to the reductions in the area of the seasonal water bodies in the same period. From 2015 to 2018, the standardized cumulative anomaly curves of annual mean air temperature, annual evapotranspiration, and annual precipitation showed an upward trend. Overall, the seasonal water area from 2015 to 2018 first increased and then decreased.

*2) Climate Factor Time-Series Analysis and Prediction:* The monthly climate factor data were used to establish an ARIMA model directly after a stationary test. The ARIMA model
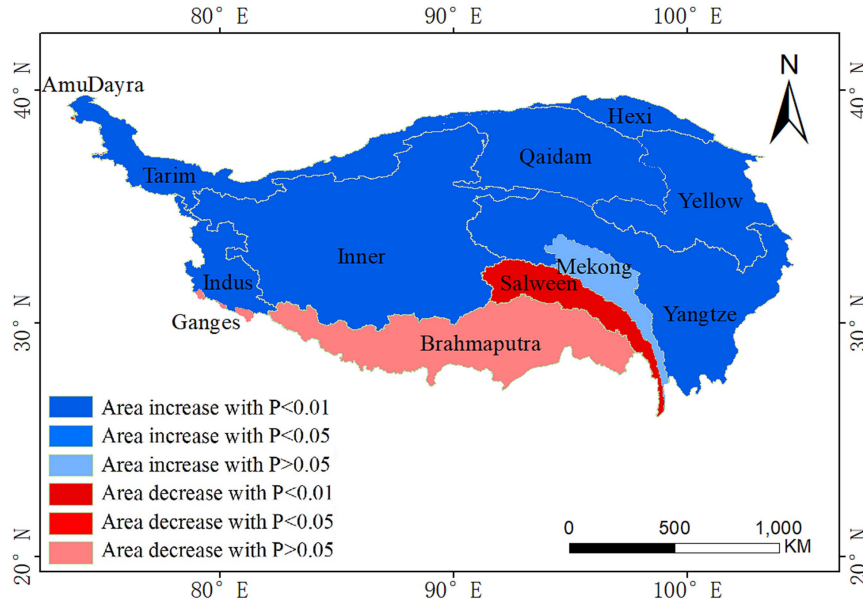
Fig. 8. Map of spatial and temporal variation trend of permanent water area in the subbasin of the QTP from 2002 to 2020.
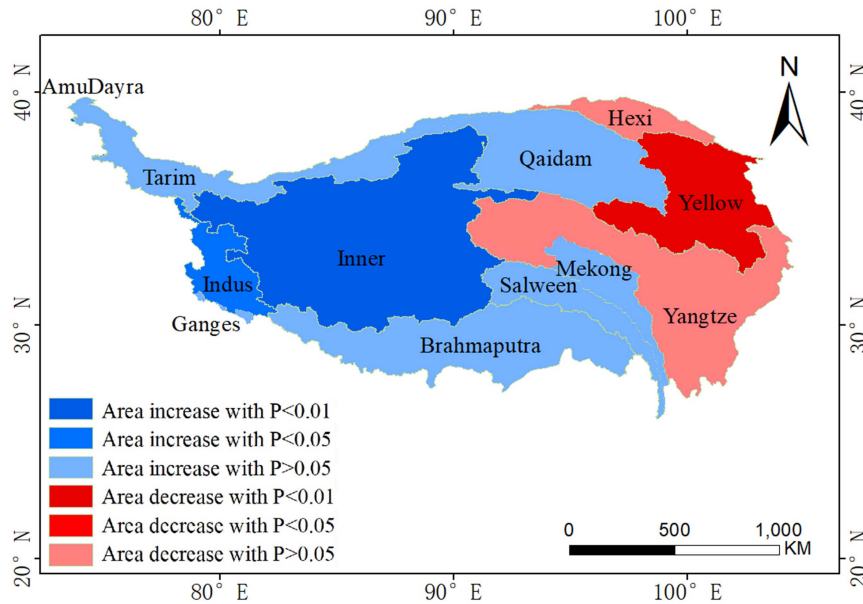


Fig. 9. Map of spatial and temporal variation trend of seasonal water area in the subbasins of the QTP from 2002 to 2020.

parameters of temperature, rainfall, and evaporation amount were set as (7, 1, 2), (8, 1, 2), (9, 1, 2). The $R^2$ of the three models were 0.975, 0.928 and 0.987, indicating that monthly change explained the temperature, precipitation, and evaporation of 97.5%, 92.8%, and 98.7%, respectively, showing that the model fitted well. The RMSE of the whole of the QTP and its 12 basins were 1.29 ° for air temperature, 9.24 mm for precipitation, and 2.88 mm for evaporation. The relative predictive error standard difference r_RMSE was 0.17 for air temperature, 0.26 for precipitation, and 0.08 for evaporation. In the ARIMA model, the evapotranspiration model had the best

fitting effect with the observed value. Fig. 13 shows the model prediction results with the example of temperature.

To illustrate the robustness of the ARIMA model, the model was retrained by replacing the input data from 2002 to 2020 by from 2002 to 2018 and from 2002 to 2019, and their predicted results were compared. Table II gives that the predicted results of temperature from January to December in 2020 using the model with different input data were very close. This indicates that the model constructed in this article had a long-time prediction ability and a good robustness. When the climatic factors of from January to December in 2020 were projected using 19
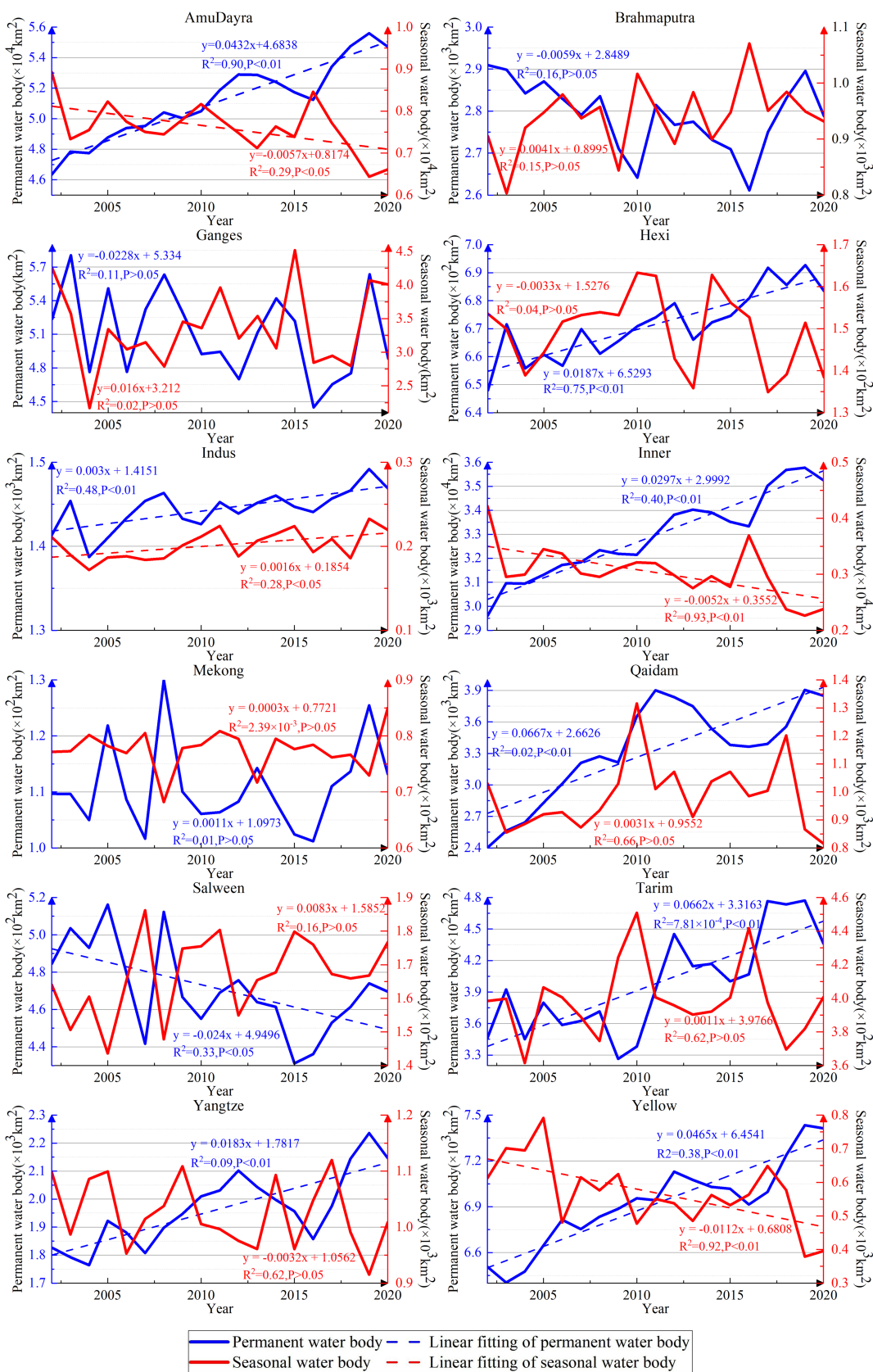
Fig. 10. Interannual change of permanent water area and seasonal water area of the subbasins in the QTP from 2002 to 2020.
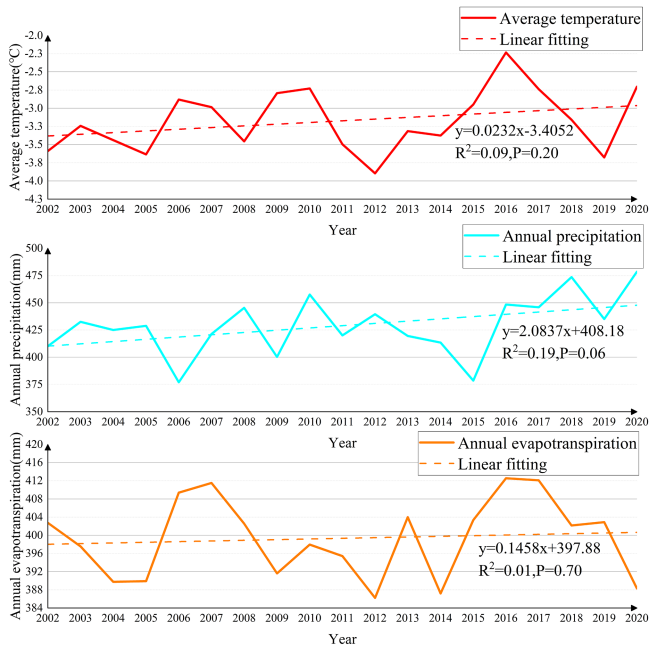
Fig. 11. Annual average temperature, total precipitation, and total evapotranspiration over the Tibetan plateau from 2002 to 2020.
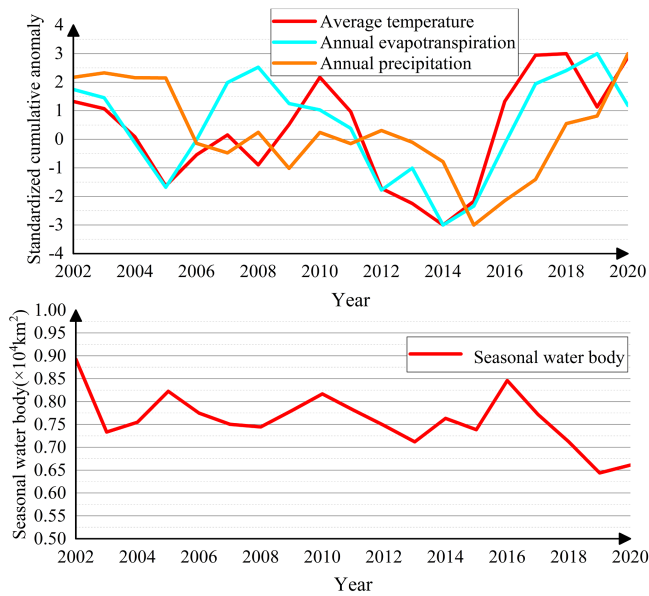


Fig. 12. Standardized cumulative anomaly curves for average temperature, annual evapotranspiration and annual precipitation (up), and the seasonal water body (down) over the Tibetan plateau from 2002 to 2020.
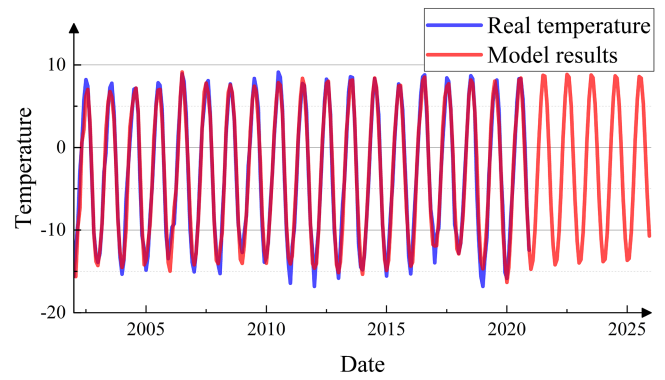


Fig. 13. Prediction results of temperature factor using ARIMA model.

TABLE II
PREDICTION RESULTS OF TEMPERATURE FACTORS OBTAINED
BY DIFFERENT MODEL INPUT

| Time | 2002 to 2018 | 2002 to 2019 | 2002 to 2020 |
|---|---|---|---|
| 202001 | -14.86 | -15.92 | -15.91 |
| 202002 | -11.63 | -12.16 | -12.18 |
| 202003 | -8.23 | -9.58 | -9.55 |
| 202004 | -3.66 | -3.65 | -3.63 |
| 202005 | 0.96 | 0.61 | 0.62 |
| 202006 | 5.33 | 4.96 | 5.01 |
| 202007 | 8.18 | 7.68 | 7.68 |
| 202008 | 7.86 | 7.90 | 7.91 |
| 202009 | 4.27 | 4.48 | 4.47 |
| 202010 | -1.65 | -1.09 | -1.16 |
| 202011 | -7.89 | -7.15 | -7.17 |
| 202012 | -11.34 | -11.93 | -11.99 |

The annual total evapotranspiration values from 2021 to 2025 were 386.54, 386.12, 385.73, 384.93, and 384.12 mm.

### D. Water Bodies and Climate Factor Correlation Analysis

*1) Permanent Water Body Area:* Fig. 14 shows that the permanent water area of AmuDayra, Bruhmaputra, and Mekong watersheds was mainly influenced by the annual mean temperature. The mean temperature of the coldest month was a major influence factor of the permanent water area in Inner and Qaidam basins, and annual total evapotranspiration was a major influence factor of the permanent water area in Indus and Salween basins. Spring mean temperature, annual total precipitation, summer and autumn total precipitation had the maximum effect on other basins.

Among the correlations between permanent water area and climate variables in each basin, the best correlation was found between permanent water area and total annual evapotranspiration in the Ganges basin, with Person coefficient of -0.72 ($p < 0.01$), and the linear fit between the two was: $y = -10^{-6}x + 0.0009$ ($p < 0.01$, $R^2 = 0.11$). Among the 13 factors, total annual evapotranspiration in the Ganges basin was the most important factor affecting the change in the permanent water area. From the time series prediction of total annual evapotranspiration in the

years of climate factor data, the prediction errors were 8.93% for air temperature, 12.83% for precipitation and 5.02% for evapotranspiration, respectively.

Based on the air temperature, precipitation and evapotranspiration data of 2002–2020, the monthly climatic factors for 2021–2025 were predicted. The annual mean temperatures for 2021–2025 were −2.557 °C, −3.078 °C, −3.173 °C, −3.030 °C, and −2.851 °C. The annual total precipitation values from 2021 to 2025 were 470.21, 470.54, 472.8, 475.08, and 477.39 mm.
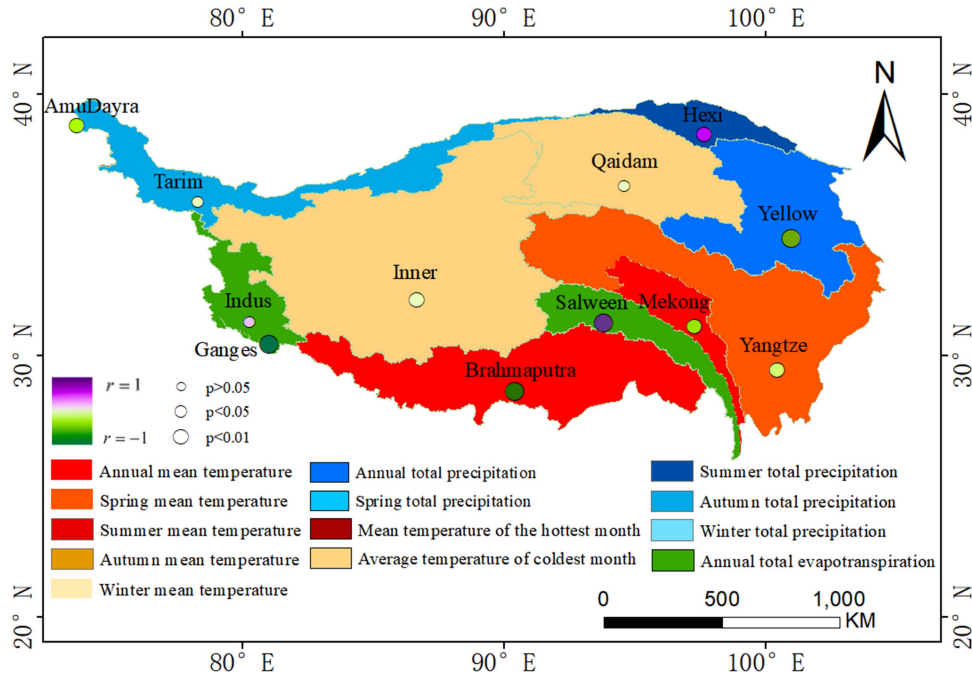
Fig. 14. Most relevant climate factor variable for the permanent water area in each basin in QTP.

Ganges basin, there is an increase of about 10 mm in total annual evapotranspiration in the basin during 2021–2025. Therefore, it can be inferred that the permanent water area in the Ganges basin in 2025 would decrease by 0.1 km$^2$ compared with that in 2020. For the whole QTP, the correlation between total precipitation and the permanent water area was the strongest. The linear fitting relationship between the total permanent water area of the QTP and the total precipitation was $y = 0.004x + 3.3421$ ($p = 0.06$, $R^2 = 0.19$). According to the ARIMA climate factor time-series model, the total precipitation of the QTP would increase slowly at first and then rapidly during 2021–2025. Therefore, the total permanent water area of the QTP would increase by 294 km$^2$ in 2025 compared with 2020.

*2) Seasonal Water Body Area:* Fig. 15 shows that the seasonal water area of the Ganges, Qaidam, and Salween basins was mainly affected by annual total evapotranspiration. The autumn total precipitation was a major influence factor of the seasonal water area in Tarim and Hexi basins, and autumn mean temperature was a major influence factor of the seasonal water area in Indus and Mekong basins. The other basins were mainly affected by annual mean temperature, spring mean temperature, summer mean temperature, spring and winter total precipitation.

Among the correlations between seasonal water area and climatic factors in each watershed, the best correlation was found between seasonal watershed area and total spring precipitation in Brahmaputra watershed, with Person coefficient of 0.58 ($p < 0.01$), and the linear fit between the two was: $y = 0.0002x + 0.0707$ ($p < 0.01$, $R^2 = 0.23$). The total spring precipitation in the Brahmaputra watershed was the most important factor affecting the change in seasonal watershed area. From the time series prediction of total spring precipitation in the Brahmaputra watershed, it was concluded that the total spring precipitation

in the watershed showed a steady-decreasing-increasing trend during 2021–2025. Therefore, it can be inferred that the seasonal watershed area of Brahmaputra watershed will first decrease by about 20 km$^2$ and then increase by about 80 km$^2$ during 2021–2025. For the entire QTP, the autumn mean temperature and seasonal water area were most relevant. The linear fitting relationship between the overall seasonal water area and the autumn mean temperature of QTP was $y = -0.0221x + 0.7034$ ($p = 0.13$, $R^2 = 0.13$). According to the ARIMA climate factor time-series model, the autumn mean temperature in the whole QTP showed a trend of decreasing first and then increasing. Therefore, the seasonal water area in QTP will reach its peak value in 2023, increasing by 131 km$^2$ compared to 2020, and decreasing by 203 km$^2$ in 2025.

## V. DISCUSSION

### A. Water Body Extraction From Time-Series Landsat Data

Landsat series satellites provided abundant RS data, which can realize long-term series and large-scale regional studies. Our results proved that the MNDWI index had a high accuracy in the extraction of water bodies from Landsat series data in QTP, and these data were of great significance for the analysis of long-term spatiotemporal changes and attribution of QTP water bodies. However, there are some limitations. In terms of surface water extraction based on MNDVI, identifying very small water areas in the image remained difficult. How to achieve large-scale, multitemporal water extraction more quickly and accurately is the direction to of future research. In the future research work, water extraction based on artificial intelligence method can be explored to improve the water extraction accuracy in the QTP. In terms of time frequency synthesis, the water body area of the
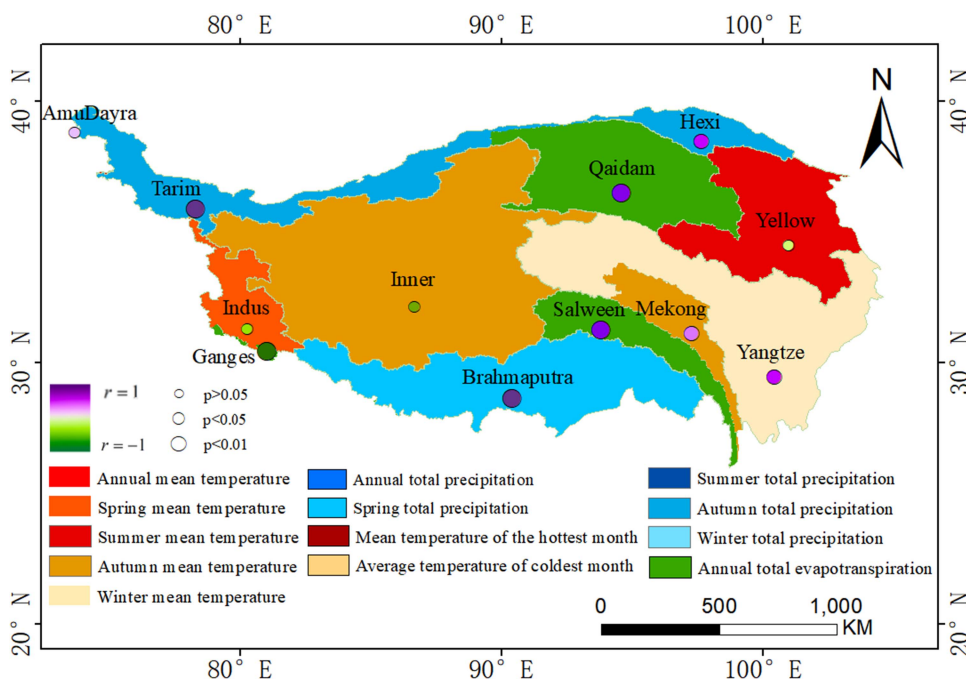
Fig. 15. Most relevant climate factor variable for the permanent water area in each basin in QTP.

Qinghai Lake is continuously increasing, which also means that the permanent water bodies area is continuously increasing. According to the calculation method of WOF, some confusion will be between permanent water bodies and seasonal water bodies. Other areas of the QTP may have the same problem. The calculation and classification methods for permanent water bodies and seasonal water bodies need be further improved and optimized.

### B. Cumulative Climate Effects on Seasonal Water Bodies

The water volume of the lake over the QTP was mainly controlled by the melting of ice and snow, the melting of permafrost, precipitation and evaporation [59]. The supplementary effect of melting water from ice, snow and permafrost aroused by temperature rise, the supplementary effect of precipitation on lake water volume, and the consumption effect of evapotranspiration on water volume were all different in a period of time. In Fig. 12, the standardized cumulative distance level curves of annual average temperature, annual evapotranspiration and annual precipitation from 2015 to 2018 show an increasing trend, which reflects a strong regularity and typicality, so the seasonal water body area in this period is further analyzed. The seasonal water area increase could be attributed to the transformation of nonwater or permanent water regions into seasonal water regions. The cause of reduced seasonal water could be summed up as the seasonal water region converted into nonwater or permanent water region, see Fig. 16. Based on change of the seasonal water area, this period was divided into two parts (i.e., 2015–2016 and 2016–2018) to analyze the impact of climate factors on the seasonal water area. The increase in seasonal water area in 2015–2016 was mainly due to the evolution of the permanent water region into seasonal water region, and
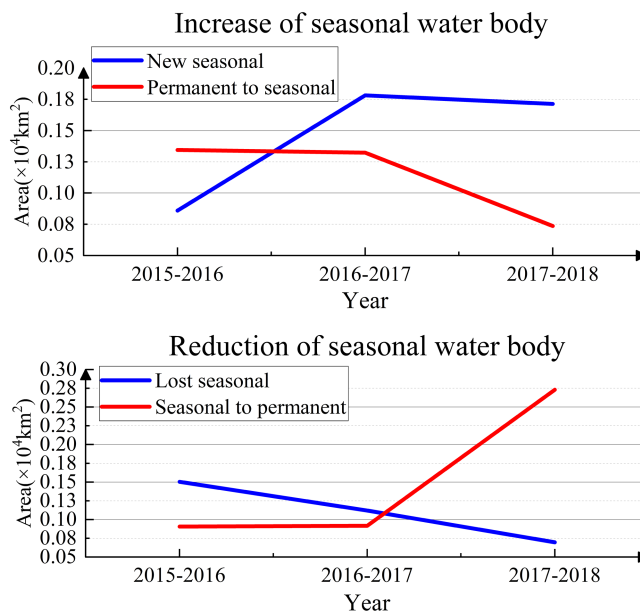


Fig. 16. Seasonal water conversion in QTP from 2015 to 2018.

the variation area reached 1345 km$^2$, accounting for 61.01% of the increased seasonal water area. The decreased seasonal water area in 2016–2018 was mainly because of the evolution of seasonal water regions into permanent water regions, and the variation area reached 3649 km$^2$, accounting for 66.76% of the decrease in seasonal water area. In general, the changes in the water body area aroused by climate factor in 2015–2018 were interconversion of seasonal water bodies and permanent water bodies.

## C. Correlation Analysis Between Water Bodies and Climatic Factors

In the analysis of the water body types and climatic factors changes, 13 typical climate factor variables were calculated considering seasonal differences, which are used for screening out the factors with the greatest correlation with the changes in the area of various types of water bodies [60], [61]. The area of various water body types in different basins would be affected by the different climate factor variables. Moreover, this study tried to predict the future changes of various water bodies using climate factor forecast through data mining. However, although the factor with the greatest correlation was selected, the absolute value of the maximum correlation coefficient was only 0.778 in solving the correlation coefficient with various water bodies areas in each basin. The correlation coefficients in some basins are relatively low because the changes of the water body area in the basin were not evident or influenced by multiple factors. In the future, multifactor combination methods would be considered for improving the correlation coefficient between climatic factors and various water bodies in each basin to carry out a high-precision water body-type area change prediction. The variation of the water body area is also related to the permafrost covering a wide area of the QTP and topographic relief, which needs further study.

## VI. Conclusion

This article investigated the temporal and spatial variation of water bodies, and their climate drivers in the QTP from 2002 to 2020. First, the water information of 12 subbasins of the QTP was extracted from the long-term time-series Landsat data. The transformation between different types of water bodies and the spatial–temporal variation trend were analyzed. In addition, the main driving factors of changes of permanent water bodies and seasonal water bodies were explored using 13 climatic variables. The main conclusions were as follows:

1) The water extraction method based on MNDWI combined with JRC water dataset products had high accuracy, and the overall accuracy was more than 97% over the QTP. The annual WOF data synthesized by time-series data could reflect not only the spatial distribution of water bodies, but also the frequency of water bodies in time.
2) The surface water body of the QTP was more in the north and less in the south, and more in the west and less in the east. Seasonal water bodies were often accompanied by the surrounding areas of the lakes and two sides of the river. The permanent water area changed from about $46\,300\,km^2$ to about $54\,700\,km^2$, and the seasonal water area changed from about $8900\,km^2$ to about $6600\,km^2$, presenting a fluctuating downward trend. According to the temporal and spatial variation results of the subbasins of the QTP, permanent and seasonal water areas were increasing in most basins, and only a few basins located in the southern and eastern parts of the QTP were decreasing.
3) From 2002 to 2020, the annual mean temperature, annual total precipitation, and annual evapotranspiration over the QTP showed oscillatory fluctuations, and the annual mean

or total amount generally showed an upward trend. The increase trend of annual mean temperature was the most apparent, reaching 0.0232 °C/a, which was also synchronous with that of annual evapotranspiration. The ARIMA model was used to analyze and predict the climate data from 2002 to 2020, and 60 monthly data were obtained for temperature, precipitation, and evapotranspiration from 2021 to 2025.
4) Among 12 subbasins in the QTP, the Pearson correlation coefficient between permanent water area and annual evapotranspiration in Gange basin was the largest, reaching $-0.72$ ($p < 0.01$). The Pearson correlation coefficient between seasonal water area and total spring precipitation in Brahmaputra basin was the largest, reaching 0.58 ($p < 0.01$).
5) The total permanent water area of the QTP would show a slow and then fast increasing trend during 2021–2025. Compared with 2021, the total permanent water area of the QTP would increase by 294 $km^2$ in 2025. The seasonal water area would increase by 131 $km^2$ and decrease by 203 $km^2$. The permanent water area in Gange basin might decrease by 0.1 $km^2$ and then remain stable in 2021–2025. The seasonal water area of the Brahmaputra basin might show a trend of stabilizing at first, decreasing by about 20 $km^2$, and then increasing by about 80 $km^2$ in 2021–2025.

## References

[1] G. Yin, F. Niu, Z. Lin, J. Luo, and M. Liu, "Effects of local factors and climate on permafrost conditions and distribution in Beiluhe basin, Qinghai-Tibet plateau, China," *Sci. Total Environ.*, vol. 581, pp. 472–485, 2017.

[2] K. Scholz, A. Hammerle, E. Hiltbrunner, and G. Wohlfahrt, "Analyzing the effects of growing season length on the net ecosystem production of an alpine grassland using model–data fusion," *Ecosystems*, vol. 21, no. 5, pp. 982–999, 2018.

[3] L. Feng, C. Hu, X. Chen, X. Cai, L. Tian, and W. Gan, "Assessment of inundation changes of Poyang lake using MODIS observations between 2000 and 2010," *Remote Sens. Environ.*, vol. 121, pp. 80–92, 2012.

[4] S. Tulipani et al., "Molecular proxies as indicators of freshwater incursion-driven salinity stratification," *Chem. Geol.*, vol. 409, pp. 61–68, 2015.

[5] Y. Zhuang, P. Wang, Y. Yang, H. Shi, H. Chen, and F. Bi, "Harbor water area extraction from pan-sharpened remotely sensed images based on the definition circle model," *IEEE Geosci. Remote Sens. Lett.*, vol. 14, no. 10, pp. 1690–1694, Oct. 2017.

[6] Y. Deng, W. Jiang, Z. Tang, Z. Ling, and Z. Wu, "Long-term changes of open-surface water bodies in the Yangtze river basin based on the google earth engine cloud platform," *Remote Sens.*, vol. 11, no. 19, 2019, Art. no. 2213.

[7] R. Shi, Q. Jia, F. Wei, and G. Du, "Comprehensive evaluation of ecosystem health in pastoral areas of Qinghai–Tibet plateau based on multi model," *Environ. Technol. Innov.*, vol. 23, 2021, Art. no. 101552.

[8] M. T. Jorgenson et al., "Resilience and vulnerability of permafrost to climate change," *Can. J. Forest Res.*, vol. 40, no. 7, pp. 1219–1236, 2010.

[9] S. K. McFeeters, "The use of the normalized difference water index (NDWI) in the delineation of open water features," *Int. J. Remote Sens.*, vol. 17, no. 7, pp. 1425–1432, 1996.

[10] V. Kanakoudis, S. Tsitsifli, A. Papadopoulou, B. C. Curk, and B. Karleusa, "Water resources vulnerability assessment in the Adriatic sea region: The case of Corfu island," *Environ. Sci. Pollut. Res.*, vol. 24, no. 25, pp. 20173–20186, 2017.

[11] G. Donchyts, F. Baart, H. Winsemius, N. Gorelick, J. Kwadijk, and N. Van De Giesen, "Earth's surface water change over the past 30 years," *Nature Climate Change*, vol. 6, no. 9, pp. 810–813, 2016.

[12] A. Ogilvie et al., "Decadal monitoring of the Niger inner delta flood dynamics using MODIS optical data," *J. Hydrol.*, vol. 523, pp. 368–383, 2015.

[13] X. Wang, F. Ling, H. Yao, Y. Liu, and S. Xu, "Unsupervised sub-pixel water body mapping with sentinel-3 OLCI image," *Remote Sens.*, vol. 11, no. 3, 2019, Art. no. 327.

[14] Y. Zhuang and C. Chen, "A method for water body extraction based on the tasselled cap transformation from remote sensing images," in *Proc. 5th Int. Workshop Earth Observ. Remote Sens. Appl.*, 2018, pp. 1–5.

[15] Z. Zhang, Z. Hu, and H. Du, "Study of information extraction method of water body based on mapping satellite-1 imagery," *Proc. SPIE Multispectral, Hyperspectral, Ultraspectral Remote Sens. Technol., Techn. Appl. V*, vol. 9263, pp. 284–294, 2014.

[16] Z. Lu et al., "Application of red edge band in remote sensing extraction of surface water body: A case study based on GF-6 WFV data in arid area," *Hydrol. Res.*, vol. 52, no. 6, pp. 1526–1541, 2021.

[17] J. Wang, M. Li, L. Wang, J. She, L. Zhu, and X. Li, "Long-term lake area change and its relationship with climate in the endorheic basins of the Tibetan plateau," *Remote Sens.*, vol. 13, no. 24, 2021, Art. no. 5125.

[18] B.-C. Gao, "NDWI—A normalized difference water index for remote sensing of vegetation liquid water from space," *Remote Sens. Environ.*, vol. 58, no. 3, pp. 257–266, 1996.

[19] G. Caccamo, L. Chisholm, R. A. Bradstock, and M. Puotinen, "Assessing the sensitivity of MODIS to monitor drought in high biomass ecosystems," *Remote Sens. Environ.*, vol. 115, no. 10, pp. 2626–2639, 2011.

[20] H. Xu, "Modification of normalised difference water index (NDWI) to enhance open water features in remotely sensed imagery," *Int. J. Remote Sens.*, vol. 27, no. 14, pp. 3025–3033, 2006.

[21] P. Rao, W. Jiang, Y. Hou, Z. Chen, and K. Jia, "Dynamic change analysis of surface water in the yangtze river basin based on MODIS products," *Remote Sens.*, vol. 10, no. 7, 2018, Art. no. 1025.

[22] J.-F. Pekel, A. Cottam, N. Gorelick, and A. S. Belward, "High-resolution mapping of global surface water and its long-term changes," *Nature*, vol. 540, no. 7633, pp. 418–422, 2016.

[23] M. G. Tulbure, M. Broich, S. V. Stehman, and A. Kommareddy, "Surface water extent dynamics from three decades of seasonally continuous landsat time series at subcontinental scale in a semi-arid region," *Remote Sens. Environ.*, vol. 178, pp. 142–157, 2016.

[24] L. A. Mason et al., "Fine-scale spatial variation in ice cover and surface temperature trends across the surface of the Laurentian great lakes," *Climatic Change*, vol. 138, no. 1, pp. 71–83, 2016.

[25] X. Dai, X. Yang, M. Wang, Y. Gao, S. Liu, and J. Zhang, "The dynamic change of Bosten lake area in response to climate in the past 30 years," *Water*, vol. 12, no. 1, pp. 1–23, 2019.

[26] Z. Tan and J. Jiang, "Spatial–temporal dynamics of wetland vegetation related to water level fluctuations in poyang lake, China," *Water*, vol. 8, no. 9, 2016, Art. no. 397.

[27] H. Kaur et al., "Predicting water availability in water bodies under the influence of precipitation and water management actions using VAR/VECM/LSTM," *Climate*, vol. 9, no. 9, 2021, Art. no. 144.

[28] Y. Bo et al., "Three decades of gross primary production (GPP) in China: Variations, trends, attributions, and prediction inferred from multiple datasets and time series modeling," *Remote Sens.*, vol. 14, no. 11, 2022, Art. no. 2564.

[29] X. Liu and K. Wu, "A preliminary study on environmental response of the water body in Chaohu lake to reginal climate change," in *Proc. 2nd Int. Conf. Asian-Eur. Environ. Technol. Knowl. Transfer*, 2008, pp. 374–377.

[30] G. Lid, F. W. Schwartz, B. Zhang, and Z. Yu, "Modelling the hydrological response of Prairie pothole water bodies to climate variability," *IAHS-AISH Publ.*, vol. 341, pp. 79–88, 2011.

[31] X. Geets, J. A. Lee, A. Bol, M. Lonneux, and V. Grégoire, "A gradient-based method for segmenting FDG-PET images: Methodology and validation," *Eur. J. Nucl. Med. Mol. Imag.*, vol. 34, no. 9, pp. 1427–1438, 2007.

[32] H. Zhu et al., "Regional characteristics of long-term variability of summer precipitation in the Poyang lake basin and possible links with large-scale circulations," *Atmosphere*, vol. 11, no. 10, 2020, Art. no. 1033.

[33] R. A. Assel, "Great lakes ice cover, first ice, last ice, and ice duration, winters 1973-2002," Great Lakes Environ. Res. Lab. U.S. Dept. Commerce Nat. Oceanographic Atmospheric Admin., 2003, pp. 7–14.

[34] C. M. O'Reilly et al., "Rapid and highly variable warming of lake surface waters around the globe," *Geophys. Res. Lett.*, vol. 42, no. 24, pp. 10,773–10,781, 2015.

[35] J. Li et al., "Satellite detection of surface water extent: A review of methodology," *Water*, vol. 14, no. 7, 2022, Art. no. 1148.

[36] D. Labat, Y. Goddéris, J. L. Probst, and J. L. Guyot, "Evidence for global runoff increase related to climate warming," *Adv. Water Resour.*, vol. 27, no. 6, pp. 631–642, 2004.

[37] A. Li, C. Xia, C. Bao, and G. Yin, "Using MODIS land surface temperatures for permafrost thermal modeling in Beiluhe basin on the Qinghai-Tibet plateau," *Sensors*, vol. 19, no. 19, 2019, Art. no. 4200.

[38] Z. Lin et al., "High spatial density ground thermal measurements in a warming permafrost region, Beiluhe basin, Qinghai-Tibet plateau," *Geomorphology*, vol. 340, pp. 1–14, 2019.

[39] W. W. Immerzeel, L. P. Van Beek, and M. F. Bierkens, "Climate change will affect the asian water towers," *Science*, vol. 328, no. 5984, pp. 1382–1385, 2010.

[40] J. Luo, G. Yin, F. Niu, Z. Lin, and M. Liu, "High spatial resolution modeling of climate change impacts on permafrost thermal conditions for the Beiluhe basin, Qinghai-Tibet plateau," *Remote Sens.*, vol. 11, no. 11, 2019, Art. no. 1294.

[41] Y. Deng et al., "Spatio-temporal change of lake water extent in Wuhan urban agglomeration based on landsat images from 1987 to 2015," *Remote Sens.*, vol. 9, no. 3, 2017, Art. no. 270.

[42] T. Long et al., "30 m resolution global annual burned area mapping based on landsat images and google earth engine," *Remote Sens.*, vol. 11, no. 5, 2019, Art. no. 489.

[43] D. Yang, W. Wang, and T. Hong, "A historical weather forecast dataset from the European centre for medium-range weather forecasts (ECMWF) for energy forecasting," *Sol. Energy*, vol. 232, pp. 263–274, 2022.

[44] D. P. Dee et al., "The ERA-interim reanalysis: Configuration and performance of the data assimilation system," *Quart. J. Roy. Meteorol. Soc.*, vol. 137, no. 656, pp. 553–597, 2011.

[45] G. Tang, Y. Ma, D. Long, L. Zhong, and Y. Hong, "Evaluation of GPM day-1 IMERG and TMPA version-7 legacy products over mainland China at multiple spatiotemporal scales," *J. Hydrol.*, vol. 533, pp. 152–167, 2016.

[46] G. Skofronick-Jackson et al., "The global precipitation measurement (GPM) mission for science and society," *Bull. Amer. Meteorol. Soc.*, vol. 98, no. 8, pp. 1679–1695, 2017.

[47] X. Sun, J. Wang, L. Zhang, C. Ji, W. Zhang, and W. Li, "Spatial downscaling model combined with the geographically weighted regression and multifractal models for monthly GPM/IMERG precipitation in Hubei province, China," *Atmosphere*, vol. 13, no. 3, 2022, Art. no. 476.

[48] J. C. Campos, N. Sillero, and J. C. Brito, "Normalized difference water indexes have dissimilar performances in detecting seasonal and permanent water in the Sahara–Sahel transition zone," *J. Hydrol.*, vol. 464, pp. 438–446, 2012.

[49] J. Cohen, "A coefficient of agreement for nominal scales," *Educ. Psychol. Meas.*, vol. 20, no. 1, pp. 37–46, 1960.

[50] Z. Zou et al., "Divergent trends of open-surface water body area in the contiguous United States from 1984 to 2016," *Proc. Nat. Acad. Sci.*, vol. 115, no. 15, pp. 3810–3815, 2018.

[51] X. Wang et al., "Gainers and losers of surface and terrestrial water resources in China during 1989–2016," *Nature Commun.*, vol. 11, no. 1, pp. 1–12, 2020.

[52] C. Bombardier et al., "Derivation of the SLEDAI. A disease activity index for lupus patients," *Arthritis Rheumatism, Official J. Amer. College Rheumatol.*, vol. 35, no. 6, pp. 630–640, 1992.

[53] F. Wei, *Modern Climate Statistical Diagnosis and Prediction Techniques*. Beijing, China: Meteorological Press, 1999.

[54] C. Li, A. K. Sampene, F. O. Agyeman, B. Robert, and A. L. Ayisi, "Forecasting the severity of COVID-19 pandemic amidst the emerging SARS-CoV-2 variants: Adoption of ARIMA model," *Comput. Math. Methods Med.*, vol. 2022, pp. 1–17, 2022.

[55] P. Mulomba Mukadi and C. González-García, "Time series analysis of climatic variables in peninsular Spain. Trends and forecasting models for data between 20th and 21st centuries," *Climate*, vol. 9, no. 7, 2021, Art. no. 119.

[56] K. ArunKumar, D. V. Kalaga, C. M. S. Kumar, G. Chilkoor, M. Kawaji, and T. M. Brenza, "Forecasting the dynamics of cumulative COVID-19 cases (confirmed, recovered and deaths) for top-16 countries using statistical machine learning models: Auto-regressive integrated moving average (ARIMA) and seasonal auto-regressive integrated moving average (SARIMA)," *Appl. Soft Comput.*, vol. 103, 2021, Art. no. 107161.

[57] K. ArunKumar, D. V. Kalaga, C. M. S. Kumar, M. Kawaji, and T. M. Brenza, "Comparative analysis of gated recurrent units (GRU), long short-term memory (LSTM) cells, autoregressive integrated moving average (ARIMA), seasonal autoregressive integrated moving average (SARIMA) for forecasting COVID-19 trends," *Alexandria Eng. J.*, vol. 61, no. 10, pp. 7585–7603, 2022.

[58] S. Dong, X. Xue, Q. You, and F. Peng, "Remote sensing analysis of lake area change in Qinghai Tibet plateau in recent 40 years," *Lake Sci.*, vol. 26, no. 4, pp. 535–544, 2014.

[59] F. Meng, F. Su, Y. Li, and K. Tong, "Changes in terrestrial water storage during 2003–2014 and possible causes in Tibetan plateau," *J. Geophys. Res., Atmos.*, vol. 124, no. 6, pp. 2909–2931, 2019.

[60] H. Li, Q. Zhang, V. P. Singh, P. Shi, and P. Sun, "Hydrological effects of cropland and climatic changes in arid and semi-arid river basins: A case study from the yellow river basin, China," *J. Hydrol.*, vol. 549, pp. 547–557, 2017.

[61] A. Dai, T. Qian, K. E. Trenberth, and J. D. Milliman, "Changes in continental freshwater discharge from 1948 to 2004," *J. Climate*, vol. 22, no. 10, pp. 2773–2792, 2009.

**Fuyao Zhu** is currently working toward Graduation degree with the School of Geophysics and Geomatics, China University of Geosciences, Wuhan, China.

Her research interests include remote sensing image information extraction and analysis and remote sensing of urban ecological environment.



**Mengmeng Wang** received the B.Sc. degree in geoscience information system from the HeFei University of Technology, Hefei, China, in 2012, and the Ph.D. degree from the Institute of Remote Sensing and Digital Earth, Chinese Academy of Sciences, Beijing, China, in 2017.

He is currently an Associate Professor with the School of Geography and Information Engineering, China University of Geosciences, Wuhan, China. His main research interests include thermal infrared quantitative remote sensing and their applications on nature hazards and agriculture.



**Chen Hong** is currently working toward the Graduation degree with the S.K.Lee Honors College, China University of Geosciences, Wuhan, China, majoring in remote sensing science and technology.

She is currently conducting research on the water bodies of the Qinghai-Tibet Plateau.



**Zhengjia Zhang** received the B.Sc. degree in geoscience information system from the HeFei University of Technology, Hefei, China, in 2012, and the Ph.D. degree in microwave remote sensing from the Institute of Remote Sensing and Digital Earth, Chinese Academy of Sciences, Beijing, China, in 2017.

He is currently an Associate Professor with the School of Geography and Information Engineering, China University of Geosciences, Wuhan, China. His research interests include synthetic aperture radar (SAR) interferometric technique, time-series interferometric SAR, and their applications on nature hazards and permafrost regions.